Impact of matrix deformations on drying of granular materials

Oshri Borgman [a,1], Ran Holtzman [a,b,*]

[a] *Department of Soil and Water Sciences, The Hebrew University of Jerusalem, Rehovot 7610001, Israel*
[b] *Centre for Fluid and Complex Systems, Coventry University, Coventry, CV15FB, United Kingdom*

ARTICLE INFO

ABSTRACT

Drying of deformable porous media is encountered in soil, paints, coatings, food, and building materials. During drying, capillary forces can displace solid particles and modify invasion thresholds, opening preferential paths for air to invade. Since drying rates are crucially dependent on liquid connectivity through the porous medium, they are affected by the drying patterns. We study the interplay between solid matrix deformation and drying patterns and rates, and the impact of pore-size heterogeneity and the confining stress in a granular material. We couple a pore-scale model of drying with a particle-scale mechanical model, to capture the two-way coupling between the evolving drying pattern and solid particle displacements. Our simulations show that for a low pore-size disorder, and low confining stress, matrix deformations are favorable and lead to preferential drying patterns which maintain high drying rates. This effect is observed throughout the drying process when the disorder is low, but disappears after breakthrough for low confining stress, indicating a different mechanism by which deformation can impact drying. These results could be significant for various industrial applications, including fabrication of advanced nano-materials, where patterned drying can be used to obtain the desired structure.

1. Introduction

Drying of granular materials is essential in many natural and industrial processes, controlling soil moisture [1,2], curing of paints, coatings [3], food [4] and building materials [5], and manufacturing of ceramics [6], among others. Often, drying induces deformation of the solid matrix, which in turn affects the transport properties. This coupling between flow and deformation can have important consequences, for instance desiccation cracks in soils can facilitate preferential transport of water, nutrients and contaminants [7], and reduce the efficiency and quality of paints, ceramics and coatings [6,8].

The manner by which isothermal drying can induce matrix deformation is as follows. Evaporation reduces the liquid pressure in the pores, increasing the pressure difference (capillary pressure) across the interface between the liquid and the air which remains at atmospheric pressure. Once the capillary pressure exceeds the entry threshold of a pore, air invades it and displaces the liquid. The pressure difference across the air-liquid interface creates an imbalance of mechanical forces on the adjacent solid particles, which can lead to their displacement depending on the interplay with other forces like interparticle friction and elasticity. Such progressive deformation modifies the transport properties (pore apertures and local invasion thresholds), and can result in the emergence of preferential pathways for the invading air in both drainage [9,10] and drying [3,11].

Drying rates and patterns are intimately linked. The rate of drying remains relatively high, and fairly constant, during an initial period (the so-called "constant rate period") in which connected liquid pathways between the porous medium's interior and its open surface (the boundary between the porous medium and the outer atmosphere) are maintained, and evaporation is determined by atmospheric demand [12]. Disconnection of these pathways marks the onset of the second ("falling rate") period, when drying rates are limited by diffusion from a receding drying front through the porous medium [8,13,14]. Consequently, preferential drying maintains liquid connectivity to the surface hence higher drying rates, whereas a compact front will disrupt liquid connectivity causing a decline in drying rates earlier on [15]. Since capillary-induced deformation of the solid, granular matrix can lead to preferential invasion patterns, we expect it to impact the drying rates as well. To the best of our knowledge, this paper is the first test of this hypothesis.

The coupling of drying and deformation has been mostly studied for the case of cohesive media such as clayey soils and slurries in the context of desiccation crack formation, e.g. [1,2,8,16,17].

---

* Corresponding author at: Centre for Fluid and Complex Systems, Coventry University, Coventry, CV15FB, United Kingdom.

E-mail address: ran.holtzman@coventry.ac.uk (R. Holtzman).

[1] Current address: Géosciences Rennes, UMR CNRS 6118, Université de Rennes 1, Rennes 35042, France.

Much less attention has been given to drying-induced deformation in *non-cohesive*, confined granular materials. Discrete pore-scale numerical simulations of drying in non-cohesive materials, demonstrated the emergence of crack-like patterns [18], with a transition from a more compact (capillary fingering) to a crack-like pattern favored for a system with lower elasticity and heterogeneity [19]. Despite these advancements, our understanding of the coupling of drying and deformations in granular materials is incomplete. In particular, the link between drying *rate* and deformations remains elusive.

This paper provides a systematic examination of the two-way coupling between deformation and drying of non-cohesive granular materials. We present a discrete, pore-scale model that exposes how the external confinement and the initial pore-size disorder affect the drying patterns and rates. Our simulations show that lowering either the confinement or the initial disorder promote matrix deformation, which consequently leads to more preferential drying patterns, maintaining higher drying rates.

2. Methods

We develop here a discrete, pore-scale model of a drying granular material, where the coupling of fluid flow, drying and deformation is achieved by integrating two models: (i) a pore-network model to simulate isothermal drying [15]; and (ii) a granular mechanics model for matrix deformation induced by fluid displacement [20]. Both models provide a simplified two-dimensional (2-D) representation of the actual three-dimensional (3-D) geometry and forces, considering a horizontal domain in which the effect of gravity on the fluids and the particles is excluded. Below we provide the essential details of the two underlying models, and the manner by which they are integrated; for further details of models (i) and (ii) see [15] and [20], respectively.

2.1. Pore-network model of drying

We formulate a pore-scale model of a porous medium by dividing it into discrete cells ("pores") to which the fluid volume is assigned, connected by "throats" representing the constrictions between the pores that control the transport properties (Fig. 1). Our model accounts for the boundary layer that develops just above the open surface of the porous medium, through which vapor diffuses to the outer environment; the width of this layer sets the initial drying rate [21]. This is introduced by extending our pore-network to include a thin layer of interconnected air "cells" above the medium, and solving for vapor diffusion in the entire domain including both the porous medium and the boundary layer [22]. For simplicity, all model cells, including in the boundary layer, are referred to hereafter as pores which are connected by throats.

Vapor concentrations are obtained by enforcing mass balance in each pore i,

$$\sum_j J_{ij} A_{ij} = 0, \qquad (1)$$

where the summation is done over all neighboring pores j. Here

$$J_{ij} = -\rho_v^{\text{sat}} D \nabla \phi \big|_{ij} \qquad (2)$$

is the vapor mass flux between two adjacent pores i and j, driven by the local gradient of relative vapor concentration, $\nabla \phi|_{ij} = (\phi_j - \phi_i)/l_{ij}$, where $\phi = \rho_v/\rho_v^{\text{sat}}$ is the local vapor density ρ_v normalized by the saturated vapor density ρ_v^{sat} (so that $\phi \in (0, 1)$), and D is the binary diffusion coefficient of vapor in air. Throat ij, connecting pores i and j, has an effective cross-sectional area of $A_{ij} = \pi r_{ij}^2$, where r_{ij} is the effective throat radius. For the boundary layer we use $A_{ij} = 4a^2$, where $2a$ is the lattice spacing. The length scale for

(a)   (b)
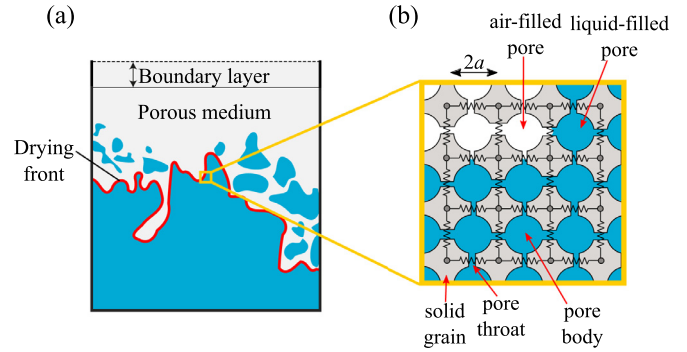
Fig. 1. (a) Model schematics. The porous medium is open at one of its faces, where a vapor concentration gradient drives evaporation from the air-liquid interface, and out to the atmosphere through a diffusive boundary layer. As evaporation reduces liquid pressure, air invades into liquid-filled pores. Some of the liquid becomes disconnected and forms isolated clusters. The drying front (in red) represents the most advancing part of the interface. (b) We model evaporation and capillary invasion via a pore network model, which we couple with a block-spring model that captures the effect of capillary pressures on matrix deformation. Pore bodies represent the space between solid particles placed on a square lattice (with spacing of $2a$), and are interconnected by throats. Solid particles are illustrated here as dented blocks, a 2-D illustration that emphasizes that our model considers a network of contact forces between particles (represented by springs), while allowing fluid connectivity between the pores. Displacement of solid particles modifies the pore throats, impacting their capillary thresholds. (For interpretation of the references to colour in this figure legend, the reader is referred to the web version of this article.)

vapor transport $l_{ij} = 2a$ in the case of neighbouring pores which are within the bulk air phase, i.e. between air-filled pores and in the boundary layer. Between pores along the air-liquid interface we set $l_{ij} = a$ to represent the shorter vapor transport path between a meniscus and the adjacent air-filled pore.

The local evaporation rate from each interface pore (Eq. (2)) is provided from the vapor concentrations in air-filled pores (Eq. (1)). For each liquid cluster (body of interconnected liquid-filled pores), we sum the local evaporation rates from all interface pores (those along the liquid-air interface, marking the cluster's edge), to obtain the total cluster's evaporation rate; multiplying by the current time step provides the total evaporated volume for that step. The overall drying rate from the entire sample is the sum of evaporation rates from all liquid clusters, and it is equivalent to the time derivative of the saturation.

The boundary conditions required to solve for vapor concentrations are as follows. We set a fixed concentration value along the air-liquid interface, $\phi_j = \phi_{\text{sat}} = 1$, and $\phi = \phi_{\text{ext}}$ (here 0) at the edge of the boundary layer. The other two domain faces are impermeable, and we set there $J = 0$. The resulting set of coupled linear equations is solved for ϕ in each air-filled pore including the boundary layer. Our model captures the reduction in evaporation rate from pores which are further away from the open surface (accounting for their larger overall diffusion length), or which are adjacent to another liquid-filled pore (a diffusion screening effect).

We use separation of timescales to simplify the computations of the liquid and vapor transport. First, we note that the timescale for liquid pressure diffusion by flow, is much shorter than that of evaporation, which here is set by the vapor diffusion (see the Supplementary Material for details). This leads to the widely-used approximation of instantaneous liquid pressure equilibration [23], such that each liquid cluster (network of connected pores) has a single uniform pressure p and meniscus curvature C, which changes instantaneously with evaporation and following pore invasion events. We further adopt the quasi-static approximation for vapour transport, using a sequence of steady-state vapour concentrations [24,25] to compute the evaporation rates excluding the effects of viscous liquid flow towards the evaporating menisci;

again, a common approximation in pore network models of drying [23,26–28]. For the case of rigid porous media, using these assumptions to model drying compared very favorably with microfluidic drying experiments [15,29].

Pore invasion and altering the fluid distribution pattern occurs when evaporation reduces the liquid pressure such that the capillary pressure—the pressure difference between the air (which remains at atmospheric pressure) and the liquid—exceeds the local capillary threshold. The spatiotemporal pressure evolution following evaporation (Eqs. (1)–(2)) is computed here as follows. In each liquid cluster the meniscus curvature C at the interface throats and the liquid pressure p are related by the Young-Laplace law, $p = -\gamma C$, where γ is the interfacial tension. We relate the meniscus curvature to the volume of liquid evaporated from it, by assuming the meniscus takes the shape of a spherical cup (for details see [15]):

$$\Delta V_{ij} = \frac{\pi (2/C)^3}{3} \left(1 - \sqrt{1 - \left(C/C_{ij}^*\right)^2}\right)^2 \left(2 + \sqrt{1 - \left(C/C_{ij}^*\right)^2}\right). \quad (3)$$

Here ΔV_{ij} is the total (cumulative) volume evaporated from a flat meniscus ($C = 0$), computed as the sum (over time) of the incremental changes in the volume of meniscus ij. Approximating each throat as a cylindrical capillary tube of radius r_{ij}, and assuming perfect wetting (vanishing contact angle), provides the critical curvature at each interface throat, $C_{ij}^* = 2/r_{ij}$. At each time step we calculate the uniform value of C in each cluster of liquid-filled pores, using $\Delta V_{tot} = \sum_{ij} \Delta V_{ij}$, where ΔV_{tot} is the total liquid volume evaporated from the cluster during that time step (obtained from Eqs. (1)–(2)), and ΔV_{ij} is computed for each interface throat (Eq. (3)). We account for the effect of liquid redistribution following pore invasion events [11,30], by redistributing the liquid volume associated with an invaded pore to all other interfacial pores in the same cluster, which decreases the cluster's curvature (according to Eq. (3)).

Simulations begin with a liquid-saturated sample. The computational algorithm is as follows: (i) the evaporation rates from the air-liquid interfaces, for a given drying pattern, are computed from Eqs. (1)–(2); (ii) the time step until the next pore invasion event is calculated from the total evaporation rate from the pores, and the evaporated volume needed to reach the next critical curvature; (iii) once an invaded pore is emptied, the pore occupancy (drying pattern) is updated; (iv) the interface curvature and liquid pressure values are calculated for each liquid cluster; (v) particle displacement and consequent modification to the throat apertures are computed. The process is repeated by returning to step (i) until breakthrough or a desired final saturation are reached.

2.2. Modeling matrix deformation and its impact on transport properties

To capture the effect of deformation on drying, we use a mechanical grain-scale model to compute the particle displacements induced by the fluid pressure variations, from which we evaluate the consequent changes to the network properties, i.e. throat apertures. The updated pore network is then used to determine the critical invasion pressure and location at the next time step. This staggering scheme—alternating between the computations of fluid flow and mechanical deformation—provides the two-way coupling between drying and matrix deformation.

Our model is 2-D in the sense that it considers interparticle forces, displacements, and fluid flow in 2-D, however it provides an essential property inherent to 3-D geometry: it allows flow between two touching particles, as fluid can still flow around the contact area. This can be illustrated by considering a square lattice of dented blocks, interconnected with springs that represent their mechanical interaction (e.g. contact forces), where the narrow constriction between the blocks (pore throats) allows fluid to flow past the contact region (Fig. 1b, see [20]). Changes in the spring contraction represent deformation of solid particles, as a result of their relative displacement (the change in position of one particle with respect to its neighbor), which also affect the throat apertures.

We consider a non-cohesive granular material, undergoing small (linearly-elastic) deformations due to particle rearrangements. Since our aim is to obtain fundamental understanding of a multiphysics problem—the interplay between evaporation, vapor and liquid transport and mechanical matrix deformation—rather than an accurate prediction for a specific system, we simplify our computations of the deformation by adopting the following assumptions. We employ the widely-used frictionless contact ("Hertzian") model, which resolves the normal, compressive component of the contact force [31,32]. This implies that the frictional forces resisting interparticle displacements are much smaller than the increment in elastic forces due to the rearrangements, which is applicable to strongly confined, densely packed particles. While friction can be important in many granular systems, to a first approximation the essential aspects of the mechanical behavior can be captured by considering the normal force component only [32,33].

In terms of the forces exerted by the fluids, we account for the capillary pressure jump across the fluid-fluid interface which pushes the particles along the interface apart, excluding the cohesive effect of interfacial tension. While the latter could significantly affect the mechanical stability of a granular packing at low humidity (due to capillary bridges that remains in inter-particle crevices after the liquid has drained from the bulk of the pore volume), its effect on advancement of the air-liquid interface is secondary to that of the capillary pressure jump [34]. This, together with the complexity of computing the magnitude and direction of the interfacial force, leads to its exclusion from pore-scale models coupling multiphase flow and mechanical deformation (e.g. [18,35]). Our model can be adapted to account for other types of materials and conditions, for example cohesion due to interparticle cement or plastic deformations, by introducing the respective mechanical constitutive relations.

Matrix deformation in response to evaporation is obtained by resolving the system's mechanical equilibrium. Here, this is provided through a force balance on each particle,

$$\sum \left(\vec{f}_p + \vec{f}_c\right) = \vec{0}, \quad (4)$$

where f_p is the force exerted by the pore fluid pressure and f_c is the interparticle contact force. The force exerted on a particle by the fluid occupying an adjacent pore body is $f_p = pA_p$, where p is the pressure in that pore, and $A_p \sim R^2$ represents the effective particle surface area upon which the pressure acts. The pressure p and force f_p are updated following evaporation of liquid and the evolution of the drying pattern (see Section 2.1). The Hertzian contact model provides a closed-form, analytical expression for the force f_c as a function of the local strain in terms of interparticle displacement h, $f_c = (4/3)\sqrt{(R/2)}Eh^{3/2}$, where E is the constrained Young modulus of the particles, and R is their radius [31]. We simplify our computations by using Taylor's expansion to obtain a piecewise linear relationship between the incremental changes in the force, $f_c(t + \Delta t) - f_c(t)$, and in the strain, $\Delta h = h(t + \Delta t) - h(t)$,

$$f_c(t + \Delta t) = f_c(t) + K\Delta h, \quad (5)$$

where $K(t)$ is the contact stiffness [20]. This is analogous to a nonlinear spring contracting by Δh, with stiffness of

$$K = 2E\sqrt{h(R/2)}. \quad (6)$$

We note that while deformation here is elastic and therefore fully reversible, the preferential pathways it creates remain open due to

the capillary pressures. Finally, the change in throat apertures at each time step, $\Delta r = r(t + \Delta t) - r(t)$ is evaluated from the relative particle displacements by

$$\Delta r = -\frac{\Delta h(1-\epsilon)}{2\sqrt{1 + (1-\epsilon)^2}}, \tag{7}$$

where $\epsilon = h(t)/2a$; this expression is obtained by considering a cubic packing of spherical particles [20].

The boundary conditions for the mechanical problem are given in the form of fixed external confinement. Here confinement is measured in terms of strains, imposed by simulating fixed, rigid walls. To highlight the effect of disorder in the flow properties, we assume that the system is initially pre-stressed homogeneously, such that all springs are subject to the same compression $h = h_0$. With this, the spatially uniform local (microscopic) strain h_0 can be linked with the macroscopic strain via $\epsilon_0 = h_0/2a$, providing the initial conditions. The above provides a linear system of equations in terms of Δh, from which we resolve the particle displacements.

2.3. Simulation parameters

The macroscopic strain ϵ_0 and throat size disorder λ are the main control parameters here. Pore-scale heterogeneity is introduced through the disorder parameter $\lambda \in (0, 1)$, which controls the distribution of pore throat apertures: at $t = 0$ (prior to the deformation), the throat radii are uniformly distributed according to $r \in [\bar{r}(1-\lambda), \bar{r}(1+\lambda)]$, where $\bar{r}$ is the average throat size. Changing λ allows us to vary the sample heterogeneity by stretching the radii distribution while maintaining the same network topology— the same spatial distribution of large and small throats. This allows us to systematically examine the impact of throat size variation without the additional effect of the specific random placement of throats. To obtain statistically representative results, for each set of parameter values (λ, ϵ_0) we generate 20 realizations (randomly varying the spatial distribution of throats). In all simulations, we keep the following parameters fixed: system size of 100×100 pores for the porous medium, a boundary layer width of $\delta = 200a$, with lattice spacing $2a = 2 \cdot 10^{-6}$ m, mean throat radius $\bar{r} = 0.4a$, particle radius $R = 1 \cdot 10^{-6}$ m, constrained Young modulus [36] $E = 1 \cdot 10^8$ N/m^2, molecular diffusion coefficient $D = 2.07 \cdot 10^{-5}$ m^2/s, interfacial tension $\gamma = 70 \cdot 10^{-3}$ N/m, and saturated density of water vapor $\rho_v^{sat} = 0.0279$ kg/m^3.

3. Results

3.1. Drying patterns

Our simulations show that lowering the initial confinement ϵ_0 and degree of disorder λ leads to more preferential drying patterns at breakthrough (when air reaches the bottom boundary), leaving significant portions of the medium wet. In the extreme case of very small ϵ_0 and λ, thin, straight fingers of dry (air-filled) pores emerge (Fig. 2). Our findings are aligned with published numerical simulations showing the effect of disorder in forced drainage [20] and drying [19], as well as experiments demonstrating the impact of confinement on drainage [9]. Experimental observations of drying patterns and rates in a non-cohesive granular material, while of great interest for future research, are outside the scope of this paper. To highlight the impact of λ and ϵ_0, in all cases presented in Fig. 2 we use the exact same initial sample geometry (spatial distribution of pore throats). In the case of low λ and ϵ_0, this causes the highly preferential patterns to emerge from the same location: the largest throat at the top surface.

The preferential drying patterns result from progressive pore opening by matrix deformation. The capillary pressure jump across
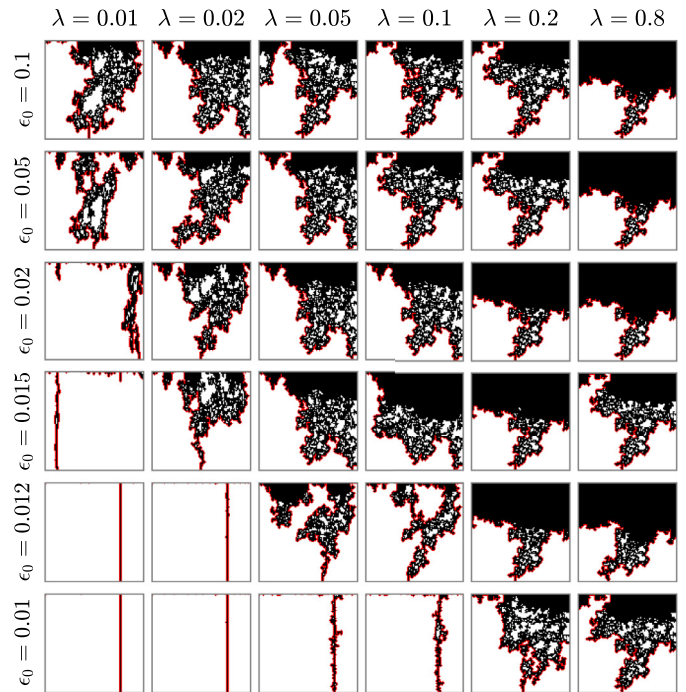

Fig. 2. Drying patterns at breakthrough, demonstrating that lowering the initial disorder in throat sizes λ and the initial confinement ϵ_0 promotes preferential drying patterns through matrix deformation, with thinner fingers of air that reach breakthrough while most of the medium is still wet. Black and white represent air- and liquid-filled pores, respectively; red line indicates the drying front. A single sample was used for all simulations in this diagram; that is, we used the exact same spatial distribution of throat sizes r (when varying ϵ_0), and the same relative magnitudes of r (when varying λ). (For interpretation of the references to colour in this figure legend, the reader is referred to the web version of this article.)

the air-liquid interface causes local force imbalance, which is equilibrated mechanically through particle displacements. The particles at the tip of the invading air finger are pushed apart, enlarging the throat apertures, cf. Eq. (7) (Fig. 3). The consequent effect on the pattern depends on the competition between the initial (undeformed) microstructural heterogeneity and the deformations. For quasi-static displacement (with negligible viscous effects) in a rigid medium, the initial microstructure dictates the drying pattern: at each step, air invasion would occur at all pores which are both accessible (along the interface) and admissible (capillary pressure meets the local thresholds). Deformations alter the local capillary thresholds, which would impact the drying pattern if these changes are sufficiently large to overcome the initial heterogeneity, namely the order of pore invasion. When this mechanism becomes dominant, a fingering instability emerges, with preferential growth at the finger tips. The resulting thin air fingers provide earlier breakthrough at higher liquid saturation.

3.2. Drying rate and time

Since the drying rate is governed by liquid connectivity to the evaporation surface [12,14], the effect of deformations on the patterns also has implications for the drying rate. Reducing the initial confinement ϵ_0, which promotes preferential drying patterns (Fig. 4a–d), results in higher drying rate, shorter time and higher liquid saturation at breakthrough (Fig. 4e–g). Fig. 4e–g shows the critical impact of confinement. For smaller ϵ_0 values particle displacements become large, and matrix deformation overcomes the pore-size disorder and dictates the drying pattern; increasing ϵ_0 reduces the deformation, such that the drying pattern is controlled by the initial, undeformed mircostructure. The patterns presented
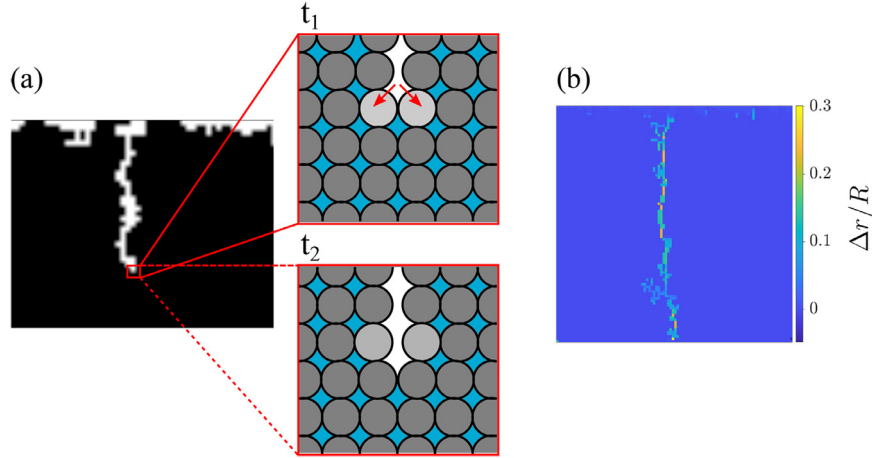
Fig. 3. Preferential drying is associated with matrix deformation. The air finger in panel (a) is the consequence of progressive pore opening due to pressure imbalance (capillary pressure) acting on the particles at the finger tip. The insets show the particle positions (gray circles), before (t_1) and after (t_2) a particular pore invasion event, featuring the enlargement of the throat formed between the particle pair (highlighted in light gray) at the finger tip due to the pressure imbalance pushing the particles apart. Red arrows indicate the resultant pressure force acting on the particles, increasing the throat aperture and facilitating the next pore invasion at the finger tip, unless a larger throat is already accessible elsewhere. Air and liquid filled pores appear in white and blue, respectively. Panel (b) shows the change in the throat apertures, Δr, rescaled by the particle radius R (for simplicity only the vertical throats are plotted). If this deformation-assisted mechanism is dominant, the macroscopic drying pattern follow the path of the modified throat apertures, making it highly preferential, leaving most of the liquid behind at breakthrough. (For interpretation of the references to colour in this figure legend, the reader is referred to the web version of this article.)
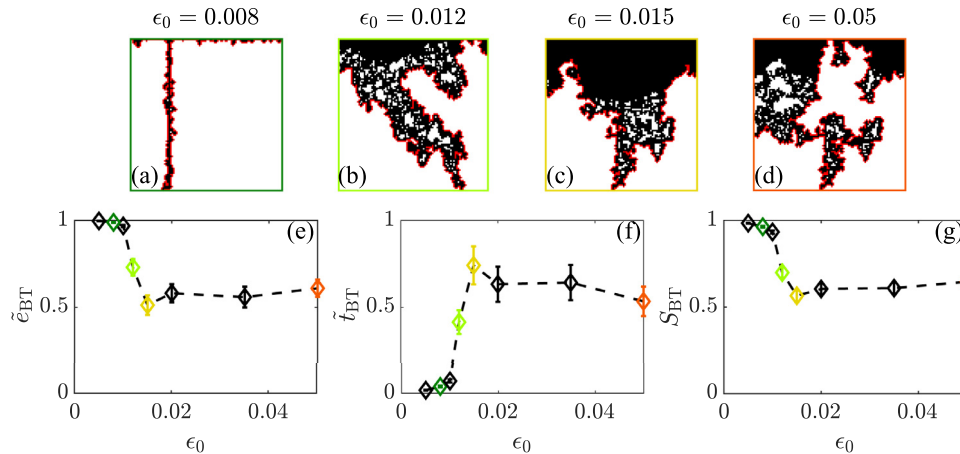

Fig. 4. Reducing the confinement ϵ_0 promotes preferential drying patterns (a–d), which result in faster drying rate, $\tilde{e}_{BT}$, shorter time, $\tilde{t}_{BT}$, and higher saturation at breakthrough, S_{BT} (e–g). Symbols and error bars in (e)–(g) represent mean values and standard error from 20 realizations for each ϵ_0, with a fixed disorder $\lambda = 0.1$. Symbol colors match those of the boxes in (a)–(d).

in Fig. 4a–d are the most representative realizations in the following sense: for each ϵ_0 value, we select the one with the saturation profile (defined here as the vertical distribution of liquid-filled pores) which is closest to the ensemble-averaged profile.

Lowering pore-size disorder λ has a similar effect to that of reducing ϵ_0: it maintains higher drying rates, with a shorter time and higher liquid saturation at breakthrough (Fig. 5e–g; panels a–d show representative patterns). Low λ amplifies the effect of small particle displacements: in a homogeneous sample, small deformations are suffice to change the arrangement of throat sizes and therefore the order of invasion. At low confinement ($\epsilon_0 = 0.01$ in Fig. 5), alteration of pore sizes by the large particle displacements overwhelms the effect of the initial disorder for low λ values, resulting in a plateau between $\lambda = 0.01$ and $\lambda = 0.1$. We stress that since the representative patterns are selected according to their saturation profile, the ensemble-averaged values may appear inconsistent with the patterns themselves. For example, the average drying rate at breakthrough for $\lambda = 0.01$ is almost similar for $\epsilon_0 = 0.01$ and 0.05 (Fig. 5e), while the chosen representative patterns in Fig. 5a differ significantly. This illustrates both the intricate link

between drying patterns and rates, e.g. the strong impact of saturation at the surface and its interplay with the diffusive boundary layer [21], as well as the importance of using ensemble averages, to avoid bias of the results due to sensitivity to the details of a specific realization.

Later on in the drying process, in particular past breakthrough, the impact of ϵ_0 becomes limited, as demonstrated by the similarity and eventually overlap of the drying rate-saturation relationship ("drying curves") for different ϵ_0 at lower saturations S (Fig. 6a), and even more so for the drying time where the effect of ϵ_0 is smaller throughout (along a wider range of S, see Fig. 6b). The drying rates show an overall larger sensitivity to λ. This is captured by a more gradual drop in drying rate for a longer duration (rate remains higher at lower S) as λ is decreased (Fig 6 c), resulting in shorter drying times (Fig. 6 d). In our analysis we use non-dimensional quantities for: (1) drying rate $\tilde{e} = e/e_0$, where e and $e_0 = (\rho_v^{sat}/\rho_l)D\phi_{sat}/\delta_{BL}$ are the absolute and potential drying rates; and (2) time $\tilde{t} = t/t_0$, where t and $t_0 = nL/e_0$ are the absolute time, and the characteristic time to evaporate all the liquid from a sample of depth L and porosity n at rate e_0.
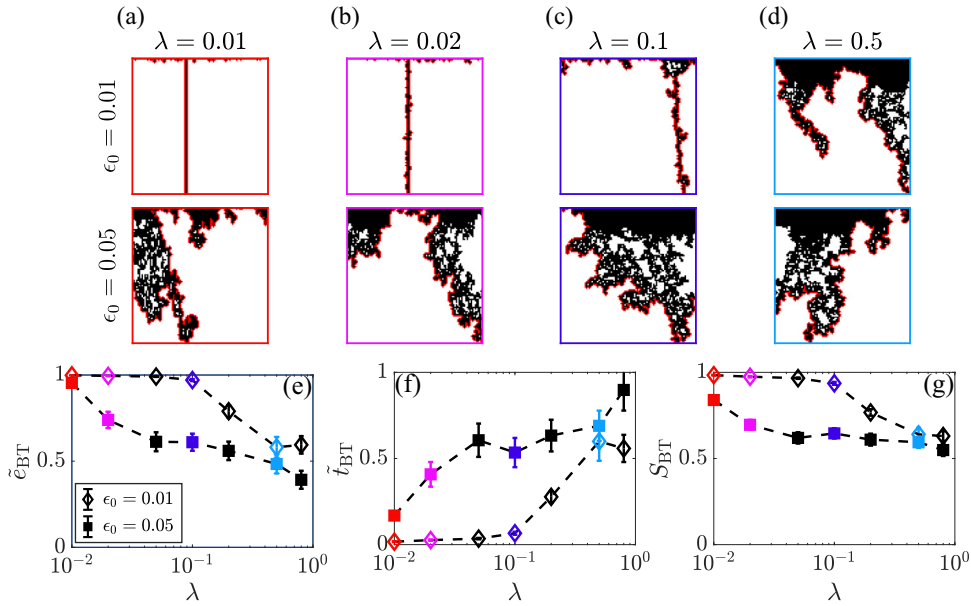
Fig. 5. Low pore-size disorder λ increases the sensitivity of drying patterns to matrix deformation, resulting in preferential drying patterns (a–d) which maintains liquid connectivity to the open surface (top of the sample). This provides higher drying rates and shorter time at breakthrough (e–f), which is achieved at higher saturation (g). Lower ϵ_0 increase the magnitude of particle displacement, thus maintaining the preferential drying behavior for higher λ. Symbols and error bars represent mean values and standard error from 20 realizations for each λ and ϵ_0. Colors of symbols match the boxes in (a)–(d).
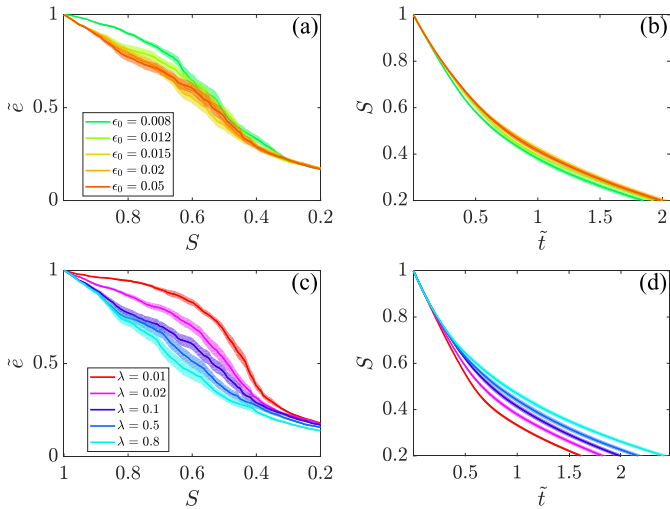
Fig. 6. Drying curves (rate vs. saturation), and the temporal evolution of the saturation. The drying rate $\tilde{e}$ decreases more gradually for lower ϵ_0 values (a), mostly in the initial stages of drying, with a relatively limited effect on $\tilde{t}$ (b). Similarly, $\tilde{e}$ decreases more gradually for lower λ (c), resulting in shorter drying time $\tilde{t}$ (d). Solid lines and shaded area represent the mean value and standard error, respectively, calculated from 20 realizations for each λ or ϵ_0 value. We use a fixed value of $\lambda = 0.1$ for the simulations in a-b, and $\epsilon_0 = 0.05$ for c-d.

4. Discussion

4.1. The impact of confinement versus disorder

Confinement affects the drying behavior in a different manner than disorder, especially past breakthrough (Fig. 6), because of the different mechanisms that are responsible for the emergence of preferential pathways in the two cases. In non-deformable media, disorder dictates the drying pattern for a quasi-static process like the one considered here. The mechanism of deformation-assisted preferential invasion relies on the deformations being sufficiently large to overcome the initial disorder. Therefore, preferential in-

vasion is favoured by both (i) reduction of the initial disorder – requiring smaller deformations to overcome them – and (ii) reduction of confinement, allowing larger deformations to take place (Fig. 7).

Since the system here remains at fixed total volume (fixed boundaries, i.e. no-strain boundary conditions), large deformations in one region prohibit further deformations elsewhere. Air fingers formed by large particle displacements (as in the case of low confinement ϵ_0) cause compaction and stiffening of the surrounding matrix (Fig. 7b, as observed experimentally [10]). This negative feedback is much less apparent at low disorder, due to the relatively small particle displacements required for the emergence of preferential pathways. Therefore, fingers continue to open even past breakthrough. As preferential invasion and the consequent connectivity of wet pores promotes faster drying, in uniform samples (low λ) a faster rate persists at later times (lower liquid saturation; Fig. 6c).

4.2. Implications of matrix deformation on drying of natural and engineered systems

Our findings improve the understanding of various drying processes in natural and engineered porous and granular systems, for instance the dependency between drying rate and deformation in soils or in paints and coatings [3], and therefore could be used to predict, control and monitor these processes. Specifically, controlling heterogeneity and confinement can be used to manipulate drying rates, as well as the amount of deformation a porous medium experiences. Manipulating heterogeneity and confinement could also be a way to produce a desired deformation pattern, which could be useful, for instance, in the manufacturing of nanomaterials [37].

In soils, matrix deformation and fracturing can impact their hydraulic properties, by changing the throat sizes and their correlation. Deformation of the granular material can change the distribution of pore sizes, and affect the permeability of the medium [38]. Opening of fracture-like pathways, provides correlated regions of connected large pores, which can become conduits for rapid transport of water and solutes by the infiltrating water, significantly en-
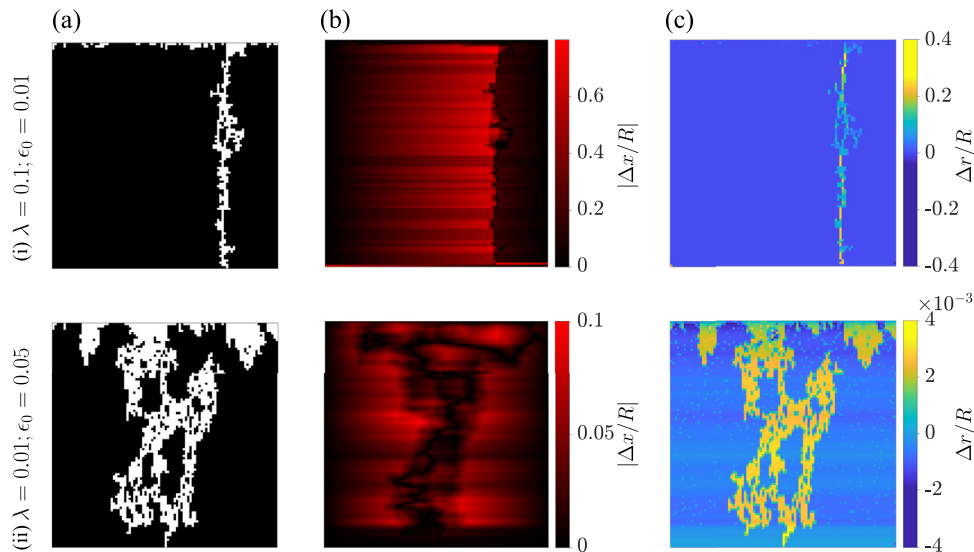
Fig. 7. Different mechanisms underlie deformation-assisted preferential drying when the deformation is induced by lowering confinement and lowering disorder: (i) Low initial confinement (top row, $\epsilon_0 = 0.01$) leads to large particle displacements and significant changes in throat apertures, while (ii) low disorder (bottom row, $\lambda = 0.01$) enhances the impact of small displacements. In both cases, the drying patterns at breakthrough are preferential (a). The magnitude of horizontal particle displacement $|\Delta x/R|$ is significantly larger for low ϵ_0 than for low λ, and centered around the invading air finger (b). Consequently, changes in vertical throat apertures $\Delta r/R$ are more pronounced for low ϵ_0 (c). We note that at low disorder, even small aperture changes impact the drying pattern, as evident from the equivalence of the pattern and deformations (panels a and c in bottom row). This is highlighted by the different scale in which the deformations are presented (panels b and c).

hancing the soil permeability. Furthermore, some of the deformation that accumulates during recurring drying and wetting cycles is irreversible, adding to the already hysteretic water retention behavior, i.e. the path-dependency of capillary pressure-saturation relationship [39].

5. Summary and conclusions

The presented model captures in a new way the coupling of drying and matrix deformation in noncohesive granular material at the pore-scale. Our simulations elucidate the impact of drying-induced matrix deformation on the drying patterns and rates. Specifically, we show that lowering the heterogeneity and the confining stress promote preferential drying patterns, due to deformation of the solid matrix, which in turn maintain liquid connectivity to the open surface of the drying sample, hence preserving higher drying rates for longer times and lower liquid saturations.

Our findings point to the different mechanisms for deformation-induced preferential drying when altering the initial disorder or the confinement. While lowering confinement simply increases the amount of deformation, lowering the disorder promotes preferential drying by enhancing the effect of small deformations. These different mechanisms also impact the long-term behavior: low confinement enhances drying rates mostly at early stages (low liquid saturations, prior to breakthrough), whereas the relatively small deformations required for preferential drying at low disorder allow for further deformations and fingering to occur past breakthrough, thus preserving higher drying rates for longer periods.

This work highlights the significant effects of capillary-induced deformations on drying, and the different roles played by the microstructure and the mechanical conditions. The presented model provides a simple yet physically-sound account of the physics underlying drying in deformable granular medium, paving the way to study drying in more complex systems where additional processes become important, for instance solute transport and reactions in cements, foods and soils.

Declaration of Competing Interest

We wish to confirm that there are no known conflicts of interest associated with this publication and there has been no significant financial support for this work that could have influenced its outcome. We confirm that the manuscript has been read and approved by all named authors and that there are no other persons who satisfied the criteria for authorship but are not listed. We further confirm that the order of authors listed in the manuscript has been approved by all of us. We understand that the Corresponding Author is the sole contact for the Editorial process (including Editorial Manager and direct communications with the office). He is responsible for communicating with the other authors about progress, submissions of revisions and final approval of proofs.

CRediT authorship contribution statement

Oshri Borgman: Conceptualization, Methodology, Software, Validation, Formal analysis, Investigation, Writing - original draft, Writing - review & editing, Visualization. **Ran Holtzman:** Conceptualization, Methodology, Software, Validation, Formal analysis, Investigation, Writing - original draft, Writing - review & editing, Supervision, Project administration, Funding acquisition.

Supplementary material

Supplementary material associated with this article can be found, in the online version, at 10.1016/j.ijheatmasstransfer.2020.119634

References

[1] H.-J. Vogel, H. Hoffmann, A. Leopold, K. Roth, Studies of crack dynamics in clay soil II. aphysically based model for crack formation, Geoderma 125 (3–4) (2005) 213–223, doi:10.1016/j.geoderma.2004.07.008.

[2] H. Peron, J. Delenne, L. Laloui, M. El Youssoufi, Discrete element modelling of drying shrinkage and cracking of soils, Comput. Geotech. 36 (1–2) (2009) 61–69, doi:10.1016/j.compgeo.2008.04.002.

[3] L. Goehring, W.J. Clegg, A.F. Routh, Plasticity and fracture in drying colloidal films, Phys. Rev. Lett. 110 (2) (2013) 24301, doi:10.1103/PhysRevLett.110.024301.

[4] T. Defraeye, A. Radu, Insights in convective drying of fruit by coupled modeling of fruit drying, deformation, quality evolution and convective exchange with the airflow, Appl. Therm. Eng. 129 (2018) 1026–1038, doi:10.1016/J.APPLTHERMALENG.2017.10.082.

[5] G.W. Scherer, Drying, shrinkage, and cracking of cementitious materials, Transp. Porous Media 110 (2) (2015) 311–331, doi:10.1007/s11242-015-0518-5.

[6] S. Kowalski, Control of mechanical processes in drying. theory and experiment, Chem. Eng. Sci. 65 (2) (2010) 890–899, doi:10.1016/j.ces.2009.09.039.

[7] M. Flury, H. Flühler, W.A. Jury, J. Leuenberger, Susceptibility of soils to preferential flow of water: a field study, Water Resour. Res. 30 (7) (1994) 1945–1954, doi:10.1029/94WR00871.

[8] L. Goehring, A. Nakahara, T. Dutta, S. Kitsunezaki, S. Tarafdar, Desiccation Cracks and Their Patterns, Wiley-VCH Verlag GmbH & Co. KGaA, 2015, doi:10.1002/9783527671922.

[9] R. Holtzman, M. Szulczewski, R. Juanes, Capillary fracturing in granular media, Phys. Rev. Lett. 108 (26) (2012) 1–4, doi:10.1103/PhysRevLett.108.264504.

[10] J.M. Campbell, D. Ozturk, B. Sandnes, Gas-driven fracturing of saturated granular media, Phys. Rev. Appl. 8 (6) (2017) 64029, doi:10.1103/PhysRevApplied.8.064029.

[11] L. Xu, S. Davies, A.B. Schofield, D.A. Weitz, Dynamics of drying in 3D porous media, Phys. Rev. Lett. 101 (9) (2008) 94502, doi:10.1103/PhysRevLett.101.094502.

[12] D. Or, P. Lehmann, E. Shahraeeni, N. Shokri, Advances in soil evaporation physics—A review, Vadose Zone J. 12 (4) (2013) 1–16, doi:10.2136/vzj2012.0163.

[13] P. Lehmann, S. Assouline, D. Or, Characteristic lengths affecting evaporative drying of porous media, Phys. Rev. E 77 (5) (2008) 056309, doi:10.1103/PhysRevE.77.056309.

[14] N. Shokri, P. Lehmann, D. Or, Liquid-phase continuity and solute concentration dynamics during evaporation from porous media: pore-scale processes near vaporization surface, Phys. Rev. E 81 (4) (2010) 46308, doi:10.1103/PhysRevE.81.046308.

[15] O. Borgman, P. Fantinel, W. Lühder, L. Goehring, R. Holtzman, Impact of spatially correlated pore-scale heterogeneity on drying porous media, Water Resour. Res. 53 (7) (2017) 5645–5658, doi:10.1002/2016WR020260.

[16] K.F. DeCarlo, N. Shokri, Salinity effects on cracking morphology and dynamics in 3-D desiccating clays, Water Resour. Res. 50 (4) (2014) 3052–3072, doi:10.1002/2013WR014424.

[17] Z. Halász, A. Nakahara, S. Kitsunezaki, F. Kun, Effect of disorder on shrinkage-induced fragmentation of a thin brittle layer, Phys. Rev. E 96 (3) (2017) 1–9, doi:10.1103/PhysRevE.96.033006.

[18] A. Kharaghani, T. Metzger, E. Tsotsas, An irregular pore network model for convective drying and resulting damage of particle aggregates, Chem. Eng. Sci. 75 (2012) 267–278, doi:10.1016/j.ces.2012.03.038.

[19] S. Kitsunezaki, Cracking condition of cohesionless porous materials in drying processes, Phys. Rev. E 87 (5) (2013) 052805, doi:10.1103/PhysRevE.87.052805.

[20] R. Holtzman, R. Juanes, Crossover from fingering to fracturing in deformable disordered media, Phys. Rev. E 82 (4) (2010) 046305, doi:10.1103/PhysRevE.82.046305.

[21] E. Shahraeeni, P. Lehmann, D. Or, Coupling of evaporative fluxes from drying porous surfaces with air boundary layer: characteristics of evaporation from discrete pores, Water Resour. Res. 48 (9) (2012) W09525, doi:10.1029/2012WR011857.

[22] J.B. Laurindo, M. Prat, Numerical and experimental network study of evaporation in capillary porous media. drying rates, Chem. Eng. Sci. 53 (12) (1998) 2257–2269, doi:10.1016/S0009-2509(97)00348-5.

[23] N. Vorhauer, Y.J. Wang, A. Kharaghani, E. Tsotsas, M. Prat, Drying with formation of capillary rings in a model porous medium, Transp. Porous Media 110 (2) (2015) 197–223, doi:10.1007/s11242-015-0538-1.

[24] A.G. Yiotis, D. Salin, Y.C. Yortsos, Pore network modeling of drying processes in macroporous materials: effects of gravity, mass boundary layer and pore microstructure, Transp. Porous Media 110 (2) (2015) 175–196, doi:10.1007/s11242-015-0529-2.

[25] M. Prat, Pore network models of drying, contact angle, and film flows, Chem. Eng. Technol. 34 (7) (2011) 1029–1038, doi:10.1002/ceat.201100056.

[26] T. Metzger, A. Irawan, E. Tsotsas, Influence of pore structure on drying kinetics: apore network study, AIChE J. 53 (12) (2007) 3029–3041, doi:10.1002/aic.11307.

[27] H. Chraïbi, M. Prat, O. Chapuis, Influence of contact angle on slow evaporation in two-dimensional porous media, Phys. Rev. E 79 (2) (2009) 026313, doi:10.1103/PhysRevE.79.026313.

[28] A. Kharaghani, T. Metzger, E. Tsotsas, A proposal for discrete modeling of mechanical effects during drying, combining pore networks with DEM, AIChE J. 57 (4) (2011) doi:10.1002/aic.12318.

[29] P. Fantinel, O. Borgman, R. Holtzman, L. Goehring, Drying in a microfluidic chip: experiments and simulations, Sci. Rep. 7 (1) (2017) 15572, doi:10.1038/s41598-017-15718-6.

[30] L. Furuberg, K.J. Måløy, J. Feder, Intermittent behavior in slow drainage, Phys. Rev. E 53 (1) (1996) 966–977, doi:10.1103/PhysRevE.53.966.

[31] K.L. Johnson, Contact Mechanics, Cambridge University Press, Cambridge, 1985, doi:10.1017/CBO9781139171731.

[32] E. Dintwa, E. Tijskens, H. Ramon, On the accuracy of the hertz model to describe the normal contact of soft elastic spheres, Granul. Matter 10 (3) (2008) 209–221, doi:10.1007/s10035-007-0078-7.

[33] I. Goldhirsch, C. Goldenberg, Stress in dense granular materials, in: The Physics of Granular Media, Wiley-VCH Verlag GmbH & Co. KGaA, Weinheim, FRG, 2005, pp. 1–22, doi:10.1002/352760362X.ch1.

[34] H.-J. Butt, M. Kappl, Normal capillary forces., Adv. Colloid Interface Sci. 146 (1–2) (2009) 48–60, doi:10.1016/j.cis.2008.10.002.

[35] A.K. Jain, R. Juanes, Preferential mode of gas invasion in sediments: grain-scale mechanistic model of coupled multiphase fluid flow and sediment mechanics, J. Geophys. Res. B: Solid Earth 114 (B8) (2009) B08101, doi:10.1029/2008JB006002.

[36] K.L. Johnson, Contact Mechanics, Cambridge University Press, 1985, doi:10.1017/CBO9781139171731.

[37] N. Chakrapani, B. Wei, A. Carrillo, P.M. Ajayan, R.S. Kane, Capillarity-driven assembly of two-dimensional cellular carbon nanotube foams, Proc. Natl. Acad. Sci. U.S.A. 101 (12) (2004) 4009–4012, doi:10.1073/pnas.0400734101.

[38] S. Bakhshian, M. Sahimi, Computer simulation of the effect of deformation on the morphology and flow properties of porous media, Phys. Rev. E 94 (4) (2016) 042903, doi:10.1103/PhysRevE.94.042903.

[39] B. Albers, Modeling the hysteretic behavior of the capillary pressure in partially saturated porous media: a review, Acta Mech. 225 (2014) 2163–2189, doi:10.1007/s00707-014-1122-4.